

Riblets Technology Application to Urban Concept Vehicle for Shell Eco-marathon Competition

Team Green Mecc, Politecnico Di Milano¹

¹IT0005001

ABSTRACT

This report presents the integration of the riblets technology to the design of a highly efficient vehicle for the Shell Eco-marathon competition. Specifically, the case study is the Urban Concept vehicle *Asteria*, designed and realized by the Team Green Mecc from Politecnico di Milano. Riblets technology, inspired by the microstructures found on sharkskin, represents a promising approach to reduce the aerodynamic drag in several engineering applications. The research work described in this report is quite innovative, as no examples of application of the riblets technology in the automotive field are found in the scientific literature. A comprehensive numerical investigation is carried out to study the effect of riblets on the vehicle drag reduction. A custom boundary condition method is adopted to accurately model the riblets effect on the vehicle surface. Computational Fluid Dynamics (CFD) simulations are performed on both vehicle models without and with riblets. The comparison of the results assesses that 2% drag reduction is achieved by using riblets technology, demonstrating their potential to enhance the efficiency of the Urban Concept *Asteria*. By considering the achieved reduction of the drag coefficient, a developed numerical model of the vehicle is exploited to estimate the improved efficiency. The energy consumption reduces by approximately 0.7%, leading to the increase in efficiency from 202.29 km/kWh (result obtained at Nogaro in 2023) to 203.7 km/kWh. A sample of 3 m² of riblets films is supplied to the team by a World leader company in riblets films production. Riblets films are placed on the most influential region of the vehicle surface, corresponding to the entire bottom area of the vehicle. The concept of applying riblets to vehicle surfaces is highly relevant to real-world applications in the automotive industry. As global regulatory increasingly prioritize energy efficiency and emission reduction, the integration of riblets technology represents a valuable approach for automotive manufacturers to enhance the environmental sustainability of their vehicles. The use of riblets on real world vehicles is unique due to its biomimetic approach. By mimicking the micro-ridged patterns, engineers can manipulate airflow over vehicle surfaces to minimize aerodynamic drag and improve energy efficiency. Unlike traditional methods of drag reduction, that mainly rely on the adoption of streamlined shapes or active aerodynamics, riblets technology offers a passive and cost-effective solution that can be applied to existing vehicle designs without significant modifications.

1 Introduction

Riblets technology, inspired by natural microstructures found on the skin of aquatic animals like sharks, is a method to reduce surface drag. As shown in Figure 2, sharks skin has a unique structure of tiny riblet-like projections, which help to reduce the frictional drag as the sharks move in the water. Riblets technology consists of microscopic streamline aligned grooves, that alter the fluid flow and lead to a reduction of the drag. Originally developed in the field of fluid dynamics to reduce the drag in watercrafts¹, riblets have now found widespread application in aerodynamics, particularly in the aviation field², and sport engineering. A number of studies have been found in the scientific literature regarding the implementation of riblets on aircraft wings³⁻⁵, ship hulls, swimsuits, and wind turbine blades⁶, to improve aerodynamic performance and overall efficiency. To the authors' knowledge there are no examples of application of riblets in the automotive industry. The present report discusses the application of the riblets technology to an highly efficient vehicle, specially designed to participate in the Shell Eco-marathon competition. To optimize the aerodynamic efficiency and minimize the energy consumption, the vehicle is fitted with a film layer of tiny riblets. The potential benefits of this solution are numerically demonstrated. The outcomes of this work lay the foundation of the potential use of riblets technology in the automotive sector to reduce fuel consumption. The Urban Concept vehicle *Asteria* (Figure 1 designed by Team Green Mecc features an optimized external shape, aimed at maximizing the aerodynamic efficiency. The frontal area is then minimized, to reduce the drag force acting on the vehicle when travelling. In particular, *Asteria* features a front section equal to $A_f = 0.908 \text{ m}^2$.

2 Theoretical background

A body moving through a fluid is subject to a drag force which consists of two main contributions: the viscous drag and the pressure drag. Viscous drag results from the frictional forces between the fluid and the surface of the body, generating a small



Figure 1. The Urban Concept Asteria, designed and realized by the Team Green Mecc from Politecnico di Milano.

region close to the wall where high-magnitude velocity gradients arise. This region is denoted as boundary layer. Rilets act upon modifying the behaviour of the fluid flow mainly in the boundary layer and, in particular, in the near-wall region. The micro-ridges or grooves of rilets interact with the boundary layer flow, inducing streamwise vortices and effectively reducing turbulent kinetic energy, which, in turn, diminishes skin friction drag.

An in-depth description of the rilets effect is given by Garcia-Mayoral and Jiménez⁷. Rilets effect is mainly local, as it depends on the local Reynolds number, based on the slip length λ , which is a characteristic parameter related to the geometrical dimensions of the rilets. The overall result involves a shift of the turbulent velocity profile in the near-wall region. This behaviour can be expressed with the introduction of the constant term ΔU^+ into the log-law as follows

$$U^+(y^+) = \frac{1}{\kappa} \ln(y^+) + A + \Delta U^+ \quad (1)$$

where $U^+(y^+)$ denotes the velocity profile of the near-wall region expressed in terms of viscous units (indicated with the superscript $+$), y^+ is the wall-normal direction, $\kappa = 0.41$ is the Von Karman constant and $A = 4.48$ is the model constant.

The velocity shift ΔU^+ is equal to the slip length expressed in viscous units λ^+ . Relevant geometrical features to assess the effect of rilets are the spacing between grooves s^+ and the square root of the nondimensional cross-section area $I_g^+ = \sqrt{A_g}$ ⁸. From previous studies, a relationship between the optimal grooves spacing s_{opt}^+ and the rilets aspect ratio A_g/s^2 is found (see Figure 4⁷). As shown in Figure 5, assuming triangular-shaped rilets, the maximum drag reduction is achieved with a spacing of $s^+ = 20$. With this result, the optimal value of the square root of the groove cross-section is computed, leading to $I_g^+ = 10.5$. It is worth noting that a further increase of the spacing of the rilets reduces the performance, leading to a drag increase when $s^+ > 30$. Moreover, it is also important to control the tip radius because its wear can highly reduce the drag decrease⁹.

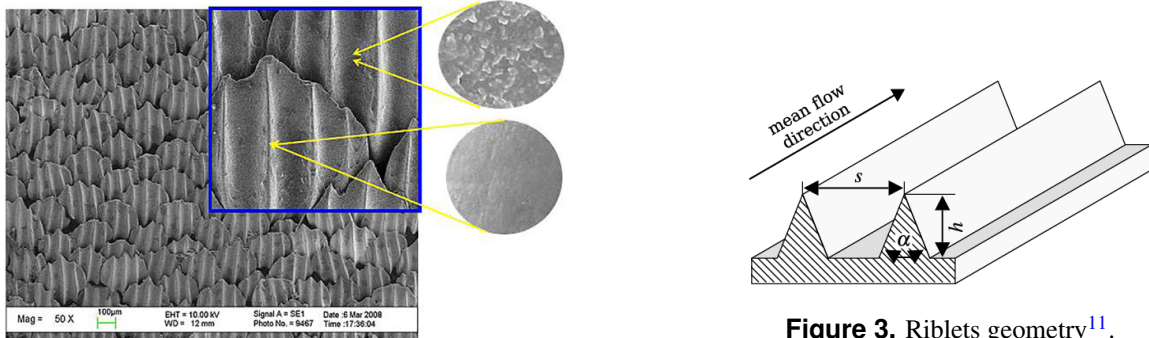


Figure 3. Rilets geometry¹¹.

Figure 2. Detail of the rilets microstructure on shark skin surface¹⁰.

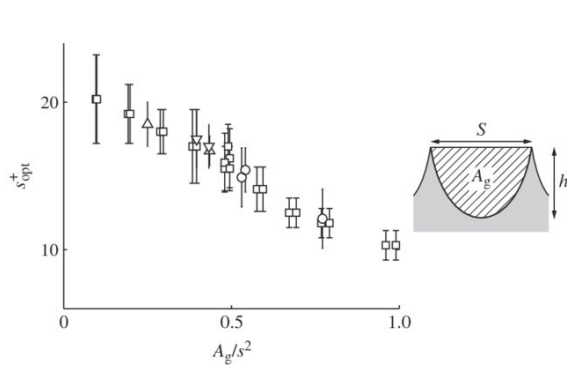


Figure 4. Optimal spacing of the riblets as function of the aspect ratio⁷.

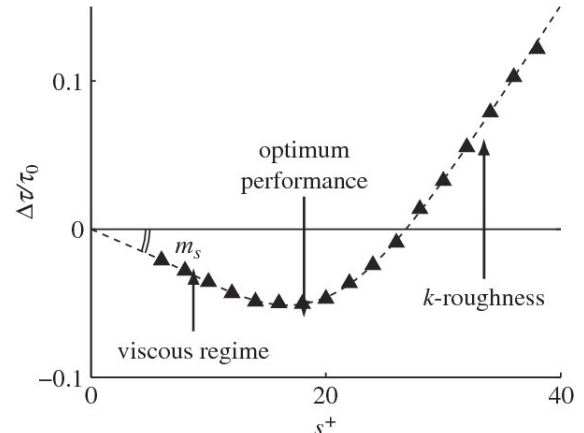


Figure 5. Drag reduction as function of the spacing s^+ for triangular-shaped riblets⁷.

3 Numerical Approach and Validation

3.1 Numerical Approach

The effect of riblets and the fluid flow features between the riblets grooves can be studied by direct numerical simulation (DNS) approach or large eddy simulation (LES) method. Due to the extremely high computational cost of these simulations methods, which are still unfeasible for problems involving complex geometries and high Reynolds numbers, an alternative method is investigated. CFD simulations based on Reynolds-Averaged-Navier-Stokes equations (RANS) are carried out, where the actual flow interaction with the riblets is not directly solved, instead it is modelled with a custom boundary condition.

Simulations are performed by exploiting the *OpenFOAM* software, as it allows to easily modify the source code and implement the riblets numerical model efficiently. The geometrical features of the modelled riblets are summarized in Table 1, with the parameters depicted in Figure 6. Since riblets can be modelled as devices which induce a partial slip condition between the body and the flow, the approach followed relies on implementing a boundary condition that models this effect on the surface. The standard slip boundary condition introduces a relationship between the tangential component of the velocity on the wall u_w and the shear rate at the wall, through the slip length λ as shown in Equation 2, which corresponds to the no-slip condition when $\lambda = 0$, and to the pure slip condition when $\lambda = 1$.

$$u_w = \lambda \left(\frac{\partial u}{\partial y} \right)_w \quad (2)$$

When dealing with the numerical problem it is necessary to introduce the discrete counterpart of Equation 2, shown in Equation 3, where u_1 is the velocity at the first cell and d is the first cell height.

$$u_w = \lambda \frac{u_1 - u_w}{d} \quad (3)$$

The relationship between λ/s and l_g^+ , which has been derived by Mele and Tognacci¹², is also necessary and it is shown in Equation 4:

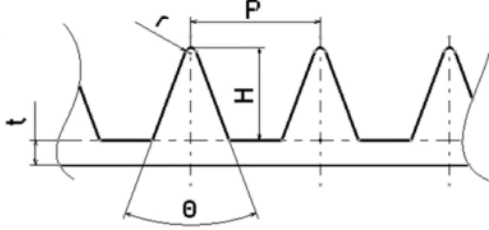
$$\frac{\lambda}{s} = \frac{C_1}{(l_g^+ - 10.5)^2 + C_2} - \lambda_0 - C_3 \cdot (l_g^+ - C_4) \cdot \frac{1}{2} \cdot (1 + \text{sgn}(l_g^+ - C_4)) \quad (4)$$

where $C_1 = 8$, $C_2 = 90$, $C_3 = 0.0023$, $C_4 = 15$, $\lambda_0 = C_1 / (10.5^2 + C_2)$.

3.2 Validation

The modified *OpenFOAM* code is validated with a 2D flat plate test case and, subsequently, the results of are compared with the ones of NASA's 2D zero pressure gradient flat plate verification case¹³. The flat plate case has been selected for validation since it is affected 100% by friction drag. The plate considered has a length $L = 2$ m, and the freestream velocity is $U_\infty = 1$ m/s, which results in a local $Re_x = 10^7$ at the end of the plate. The computational domain extends 0.3 m upstream of the plate and a symmetry boundary condition is applied in this region in order to represent a freestream approaching the flat plate.

The mesh selected for this case has 137 cells in the streamwise direction and 97 cells in the normalwise direction, with an



P	H	θ	r	t
$300\mu m$	$150\mu m$	30 deg	$5\mu m$	$210\mu m$

Table 1. Geometrical data of the modelled riblets.

Figure 6. Riblets geometry.

overall amount of 13289 cells. This mesh has been obtained from NASA's 2D zero pressure gradient flat plate verification case¹³ and it is presented in Figure 7. Considering the grid sensitivity study proposed by NASA, it is possible to notice that this mesh reduces the computational cost of the simulation drastically without significantly influencing the results, making this an efficient tool for validation of the implemented custom boundary condition.

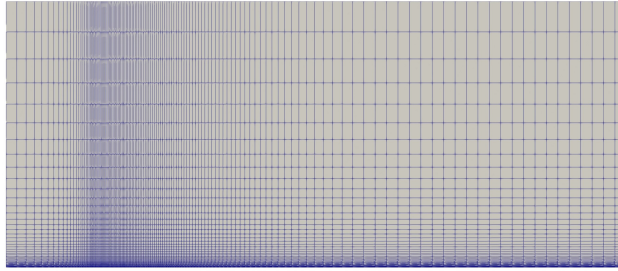


Figure 7. Structured mesh over the 2D flat plate.

The mesh setup stated above would guarantee $y^+ < 1$, and, therefore, it would be capable of capturing correctly the boundary layer. Nevertheless, doing the same thing in the complete vehicle case would be unfeasible, since the computational cost would grow extremely, leading to the need for wall functions. For this reason, wall functions have been used in both cases to ensure consistency. As discussed in section 2, the riblets have been modelled having the optimal V-shape, leading to a $l_g^+ = 10.5$. Similarly, their optimal spacing has been derived from the shear stress distribution of the car, resulting in a spacing of $\sim 300\mu m$, or $s^+ = 18$ if expressed in viscous units, and $\Delta U^+ = \lambda^+ = 1$. In Figure 8, it can be appreciated how riblets influence the streamwise evolution of the friction coefficient, resulting in a decrease of about 5% with respect to the standard case. The correctness of the model can be directly seen in Figure 9, which clearly shows the upward shift of the mean velocity profile, regardless of the streamwise location. Furthermore, the shift has a unitary value, which confirms that $\Delta U^+ = \lambda^+ = 1$. In Figure 10 and 11 it is shown the plot of the shear stress at the wall on the flat plate respectively without and with the presence of the riblets on the surface, where it is clearly visible the reduction in the wall shear stress which leads to the drag reduction.

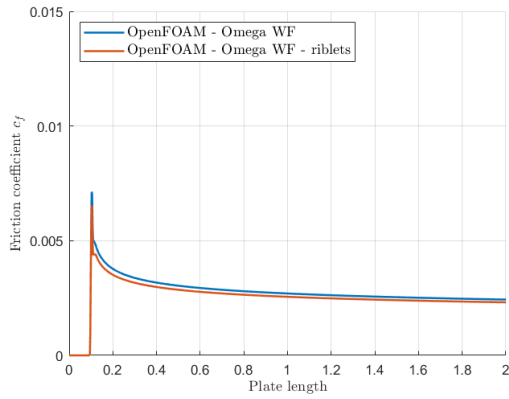


Figure 8. Evolution of the skin-friction coefficient with/without riblets.

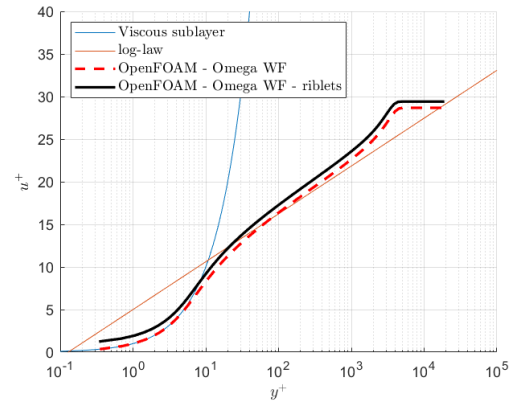


Figure 9. Mean velocity profile with/without riblets over the flat plate.



Figure 10. Wall shear stress distribution on the plate without riblets.



Figure 11. Wall shear stress distribution on the plate with riblets.

4 Effect of riblets on vehicle drag reduction

Numerical simulations are conducted using the OpenFOAM computational fluid dynamics (CFD) software package. The aim is to investigate the aerodynamic performance of the vehicle equipped with riblets technology. Simulations are performed considering both the vehicle with and without riblets. A final comparison of the results allows to asses the influence of adopting riblets on the drag reduction.

4.1 Numerical modelisation

4.1.1 Computational domain and mesh generation

In the numerical simulations, a comprehensive approach is adopted to capture the intricate flow behaviour around the vehicle equipped with riblets technology. The computational domain is built exploiting the vehicle half symmetry along the median longitudinal plane. The size of the domain is $30\text{m} \times 4\text{m} \times 6.4\text{m}$, and the vehicle is placed at 10m from the inlet surface. The developed model is shown in Figure 12. The background mesh is generated with *blockMesh* using cubic cells with size equal to 0.2m . To ensure accurate and reliable results, a mesh refinement strategy is implemented, particularly near the vehicle surfaces where flow gradients are most pronounced. The objective is to achieve a low value of y^+ (in the order of few tens). To comply with this requirement, a progressive spatial mesh refinement is implemented, decreasing the cell size step by step up towards the vehicle surface. The progressive refinement is generated with the *snappyHexMesh* utility, and six refinement boxes of different levels are placed in the most critical areas, namely the wake and the wheels regions. The mesh size is reduced from 0.2m (level 0 background mesh) to $3.125 \times 10^{-3}\text{m}$ (box with highest level of refinement). In order to properly capture the behaviour of the boundary layer and obtain an acceptable value of y^+ , 3 layers are added by setting the height of the first layer at $6.5 \times 10^{-4}\text{m}$. A mesh convergence study is performed to ensure the reliability of the results, regardless of the mesh size. The convergence analysis is carried out by gradually increasing the level of refinement in the boxes and on the surface of the vehicle. The results of the mesh convergence study are shown in Table 2. Four different types of mesh are compared, among which the super-fine is the one selected for the final analysis and post processing. Finally, Figure 13 illustrates the main refinement boxes in the finest grid case, which consists of 8.7×10^6 cells.

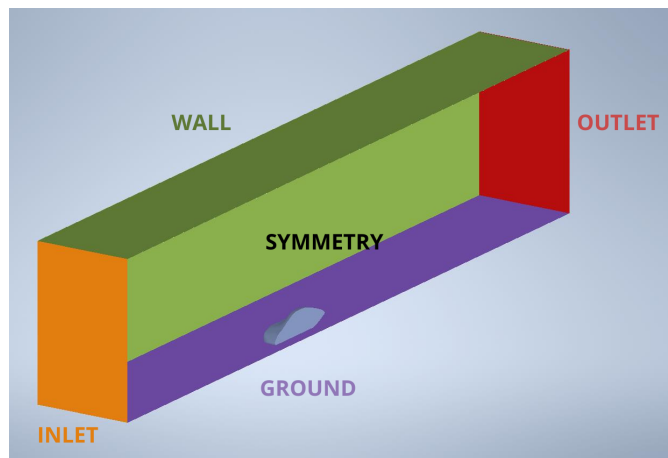


Figure 12. Computational domain.

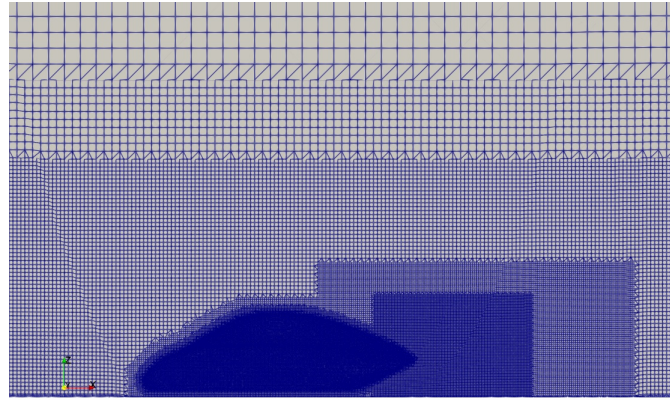


Figure 13. Refinement regions around the vehicle.

	Coarse mesh	Medium mesh	Fine mesh	Super-fine mesh
Cells number	4.7×10^5	1.5×10^6	4.4×10^6	8.7×10^6
C_D	0.1304	0.1286	0.1271	0.1213

Table 2. Results of the mesh convergence analysis.

4.1.2 Boundary conditions and turbulence model

In a CFD simulation, designating the initial and boundary conditions properly is crucial. The initial values of the simulation are shown in Table 3, where I is the turbulence intensity, which has been set to 5% corresponding to a medium-turbulent case, and C_μ is a model constant for the turbulence model.

In order to solve the RANS equations, it is necessary to model the term related to the Reynolds stress tensor. This can be done by choosing the turbulence model that is more suitable to the problem. The $k - \omega$ SST¹⁴ model, which belongs to the family of the two equations models, has been chosen for this simulation. It has been developed specifically to resolve the flow in problems that involve the presence of adverse pressure gradients and regions of separated flow. The $k - \omega$ SST model allows to blend the standard $k - \omega$ model, which is used in the near wall region, and the $k - \epsilon$ model, used in the outer region.

To ensure that the simulation is a good representation of the real problem, it is necessary to set the proper boundary conditions at the different interfaces. In addition, since it is not feasible to resolve directly the viscous sublayer, which requires a value of $y^+ < 1$, the use of wall functions is exploited. Since only half of the car is simulated, a symmetry boundary condition must be imposed on the symmetry plane, which assumes a zero flux of all the quantities across it. Table 4 shows all the boundary conditions and the wall functions employed in the simulations.

U_∞	p_∞	ω	I	κ	C_μ
10 m/s	0 Pa	9000	5 %	3.375 J	0.09

Table 3. Initial values.

Boundary	U	p	ω	κ	v_t
Car	fixedValue	zeroGradient	omegaWallFunction	kqRWallFunction	nutUSpaldingWallFunction
Tyre	rotatingWallVelocity	zeroGradient	omegaWallFunction	kqRWallFunction	nutUSpaldingWallFunction
Ground	movingWallVelocity	zeroGradient	omegaWallFunction	kqRWallFunction	nutUSpaldingWallFunction
Inlet	fixedValue	zeroGradient	fixedValue	fixedValue	zeroGradient
Outlet	inletOutlet	fixedValue	zeroGradient	zeroGradient	zeroGradient
Sides	slip	slip	slip	slip	slip
Symmetry wall	symmetry	symmetry	symmetry	symmetry	symmetry

Table 4. Boundary conditions.

4.1.3 Numerical schemes

In *OpenFOAM*, the numerical schemes are declared in the *fvSchemes* file in the system directory. Second-order accurate schemes have been used for all the quantities in the turbulence equations in order to guarantee stability and convergence. Concerning gradient scheme, the second-order accurate Gauss linear method has been used. For the divergence scheme, the linear-upwind scheme, which is a blend of the linear and upwind schemes (respectively first and second order methods), has been employed, except for the $\operatorname{div}(\phi, U)$ for which a linear scheme was selected. As interpolation scheme, the linear method has been used in order to interpolate the solution from the cell centers to the face centers. Lastly, concerning the Laplacian terms, the Gauss linear scheme has been used.

4.2 CFD simulations results

In order to face with the required high computational cost, CFD simulations are performed leveraging *Amazon Web Services (AWS) EC2* instances¹⁵. Particularly, AWS EC2 provides scalable cloud-compute capacity, offering a variety of instance types that are well-suited for high-performance computing tasks. The selected machine is reported in Table 5.

Instance type	vCPU	RAM	clock time
c5d.18xlarge	72	144 GB	3GHz

Table 5. Computational data.

Table 6 shows the comparison between the model without riblets and the model with riblets in terms of aerodynamics coefficients. In particular, the drag coefficient C_D and the lift coefficient C_L are reported. Since the simulation shows that viscous drag of the vehicle roughly represents the 35% of the total drag, and assuming the riblets only affect the shear stress, the expected drag reduction is equal to approximately 1.75%. Actually, the adoption of riblets technology also affects the flow behaviour around the vehicle body because of the different gradients. This effect is extremely shape-dependent and it cannot be estimated beforehand, thus, resulting in an overall drag reduction that may be higher or lower than the expected 1.75%. The comparative analysis shows meaningful results, with the application of riblets films leading to 2.06% drag reduction.

	C_D
No riblets	0.1213
Riblets	0.1188

Table 6. Results of the CFD simulations. Comparison of the aerodynamic drag coefficient.

Figures 14 and 15 depict the wall shear distribution of the region corresponding to the bottom surface of the rear end of the vehicle, respectively for the case without riblets and the case with riblets. This region of the vehicle corresponds to a region of separated flow. It is possible to notice that the use of riblets films has the benefit to decrease the wall shear stress in different areas, in particular on the sides and on the center part. This result demonstrates that the adopted spacing of the riblets allows to reduce the wall shear stress across its entire range.

In Figure 16, the velocity field in correspondence of the vehicle surface for the model with riblets is depicted. Due to the presence of riblets, the velocity field is not null on the vehicle surface, as it would be with the adoption of standard no-slip boundary condition. The result provided in Figure 16 demonstrates also the effectiveness of the built boundary condition.

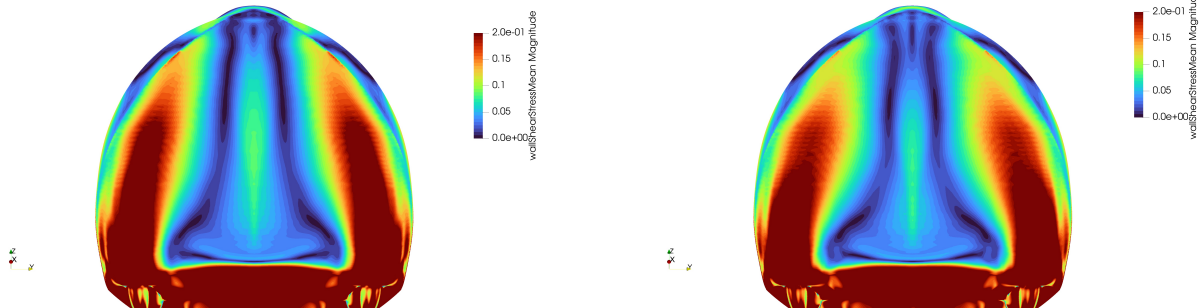


Figure 14. Wall shear stress distribution on the bottom surface of the rear end: model without riblets.

Figure 15. Wall shear stress distribution on the bottom surface of the rear end: model with riblets.

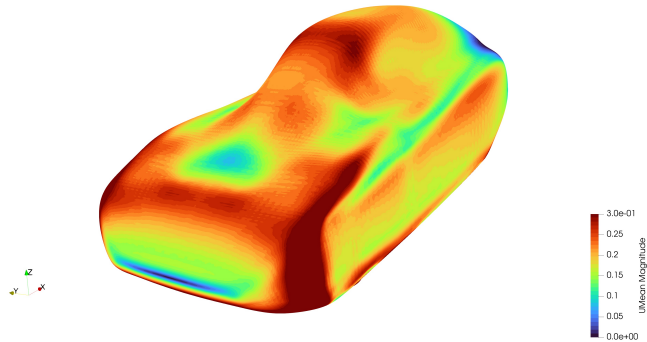


Figure 16. Velocity field at the vehicle surface for the model with riblets.

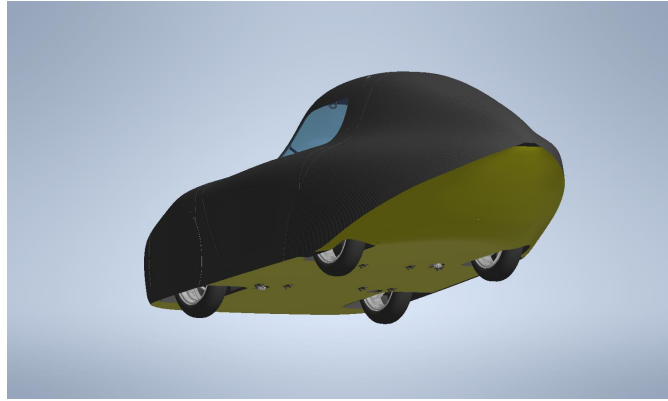


Figure 17. Region where riblets films are placed (highlighted in yellow).

5 Riblets application to Asteria Urban Concept

Riblets can be implemented in various forms, including films, coatings or directly integrated into the surface of the object. Films are the most widespread method of applying riblets. Typically, riblet films are manufactured using advanced techniques such as extrusion or casting, where a thin layer of material containing micro-ridged patterns is precisely formed. For this application, an amount of 3 m^2 of riblets films is supplied by a World leader company in riblets films production. A scheme of the supplied riblets films is depicted in Figure 18. The films consist of strips with approximate size $1100\text{ mm} \times 210\text{ mm}$. Geometrical features of the supplied riblets films are the same listed in Table 1 (see Section 3.1). Figure 19 shows an image of a supplied riblets film. The image is captured by means of an optical microscope and provides a good representation of the grooves that characterize the riblets. As shown in Figure 18, the riblets film is packaged with various layers. Since riblets films are highly susceptible to environmental factors, a protective sheet is covers the bottom surface, while a release sheet is placed on the bottom side. Both protective sheet and release sheet are removed during the laying process of the riblets. Riblets films are placed on the vehicle surface so that the grooves are aligned with the local direction of the fluid flow. Moreover, in order to guarantee the proper performance of the riblets, an high quality surface roughness is required. Specifically, the application surface requires a roughness lower than the value of grooves height (for this case study $150\text{ }\mu\text{m}$). To obtain the required surface finish, surface sanding and the use of a polymeric primer are exploited. The final roughness is verified by means of measurements with a roughness gauge. Since the quantity of supplied riblets films are not sufficient to cover the entire external surface of the vehicle, riblets are placed on the most influential regions. Based on the results of the CFD simulations, the riblets films are placed on an extended area corresponding to the bottom surface of the lower floor of the vehicle chassis and the bottom surface of the rear tail (see yellow area in Figure 17).

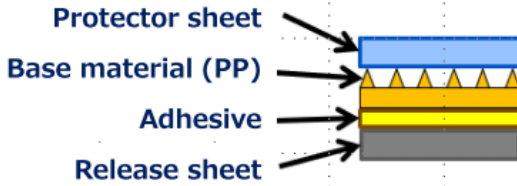


Figure 18. Detail of the cross section of the used riblets film.

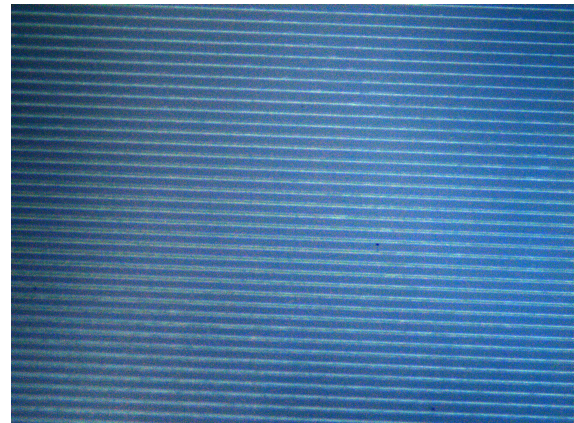


Figure 19. Detail of the used riblets film. Image captured through an optical microscope.

6 Riblets impact on real world applications

The outcomes of this work suggest that the integration of riblets technology into real-world applications within the automotive sector has significant implications for improving energy efficiency and reducing emissions. By strategically implementing riblets on vehicles surfaces, automotive manufacturers can effectively mitigate aerodynamic drag and reduce the energy consumption. Drag reduction directly contributes to reduce carbon emissions and significantly decrease greenhouse gas emissions, aligning with global efforts to face climate change and promote environmental sustainability. A simple analysis is carried out to roughly estimate the potential benefits of a large scale application of riblets. For the sake of simplicity, this analysis consider only electric vehicles. Referring to data published by the European Environment Agency¹⁶, the average European aggregated emissions in 2022 were 251 grams of CO₂ per kWh produced. Assuming the average energy consumption of an electric vehicle to be about 15 kWh/100km, and assuming a yearly mileage of 10000 km, the annual emission translates into 377 kg of CO₂ per electric car. As reported in the study by Mastinu and Ploechl¹⁷, a 10% reduction of the aerodynamic drag results in approximately a 3.5% reduction of the energy required by the vehicle. If a 2% drag reduction due to the integration of the riblets is considered, a saving of approximately 2.72 kg per year of CO₂ is achieved. According to a BloombergNEF's study on electric vehicles¹⁸, 14.1 million electric cars were present in Europe by the end of 2023. By scaling the emissions reduction on the entire electric cars fleet, the potential amount of CO₂ saving per year is more than 38000 metric tons.

7 Conclusions

The report studies the potential of riblets implementation on an highly efficient vehicle as effective strategy for reducing the aerodynamic drag. By performing CFD simulations, where a custom boundary condition is modelled to account the effect of riblets, a reduction of the drag coefficients of 2% is observed. Based on the results of the numerical simulations, the riblets technology is practically implemented on the Urban Concept vehicle *Asteria*. A significant quantity of riblets films is supplied by a World leader company in riblets films production. The films are placed on most influencial regions, namely the bottom part of the vehicle. Numerical simulations of the vehicle travelling on the Nogaro Circuit are exploited to estimate the energy consumption reduction due to the decreased drag coefficient. Results show an increase in efficiency from 202.29 km/kWh (result obtained at Nogaro in 2023) to 203.7 km/kWh. Finally, the impact of using riblets technology on large-scale automotive field is discussed. A significant reduction of the CO₂ emissions (about 38000 metric tons per year) is expected assuming the implementation of riblets on the total electric vehicle fleet in Europe.

References

- Choi, K., Gadd, G., Pearcey, H. *et al.* Tests of drag-reducing polymer coated on a riblet surface. *Appl. Sci. Res.* **46**, DOI: [10.1007/BF00404818](https://doi.org/10.1007/BF00404818) (1989).
- Cacciatori, L. *et al.* Drag reduction by riblets on a commercial uav. *Appl. Sci.* **12**, DOI: [10.3390/app12105070](https://doi.org/10.3390/app12105070) (2022).
- Viswanath, P. Aircraft viscous drag reduction using riblets. *Prog. Aerosp. Sci.* **38**, 571–600, DOI: [https://doi.org/10.1016/S0376-0421\(02\)00048-9](https://doi.org/10.1016/S0376-0421(02)00048-9) (2002).
- Bliamis, C., Vlahostergios, Z., Misirlis, D. & Yakinthos, K. Numerical evaluation of riblet drag reduction on a male uav. *Aerospace* **9**, DOI: [10.3390/aerospace9040218](https://doi.org/10.3390/aerospace9040218) (2022).

5. Bechert, D. & Hage, W. *Drag reduction with riblets in nature and engineering* (2006).
6. Chamorro, L. P., Arndt, R. & Sotiropoulos, F. Drag reduction of large wind turbine blades through riblets: Evaluation of riblet geometry and application strategies. *Renew. Energy* **50**, 1095–1105, DOI: <https://doi.org/10.1016/j.renene.2012.09.001> (2013).
7. García-Mayoral, R. & Jiménez, J. Drag reduction by riblets. *Philos. Transactions Royal Soc. A* **369**, 1412–1427, DOI: [10.1098/rsta.2010.0359](https://doi.org/10.1098/rsta.2010.0359) (2011).
8. Mele, B. & Tognaccini, R. Numerical simulation of riblets on airfoils and wings. *50th AIAA Aerosp. Sci. Meet. including New Horizons Forum Aerosp. Expo.* DOI: [10.2514/6.2012-861](https://arc.aiaa.org/doi/pdf/10.2514/6.2012-861). <https://arc.aiaa.org/doi/pdf/10.2514/6.2012-861>.
9. Mele, B., Tognaccini, R., Catalano, P. & de Rosa, D. Effect of body shape on riblets performance. *Phys. Rev. Fluids* **5**, DOI: [10.1103/PhysRevFluids.5.124609](https://doi.org/10.1103/PhysRevFluids.5.124609) (2020).
10. Pu, X., Li, G. & Huang, H. Preparation, anti-biofouling and drag-reduction properties of a biomimetic shark skin surface. *Biol. Open* **5**, DOI: <https://doi.org/10.1242/bio.016899> (2016).
11. Gatti, D., Deyn, L., Forooghi, P. & Frohnappel, B. Do riblets exhibit fully rough behaviour? *Exp. Fluids* **61**, DOI: [10.1007/s00348-020-2921-0](https://doi.org/10.1007/s00348-020-2921-0) (2020).
12. Mele, B. Riblet drag reduction modeling and simulation. *Fluids* **7**, DOI: [10.3390/fluids7070249](https://doi.org/10.3390/fluids7070249) (2022).
13. NASA. 2d zero pressure gradient flat plate verification case. <https://turbmodels.larc.nasa.gov/flatplate.html> (2013).
14. Menter, F. R. Two-equation eddy-viscosity turbulence models for engineering applications. *AIAA J.* **32**, 1598–1605 (1994).
15. Amazon. Amazon web services (2024).
16. Agency, E. E. Greenhouse gas emission intensity of electricity generation. Tech. Rep., European Environment Agency (2023).
17. Mastinu, G. & Ploechl, M. *Road and Off-Road Vehicle System Dynamics Handbook* (CRC Press, Boca Raton, 2014).
18. BloombergNEF. Electric vehicle outlook 2023. Tech. Rep., BloombergNEF (2023).